Journal of Physics and Chemistry of Solids 164 (2022) 110607

Contents lists available at ScienceDirect

Journal of Physics and Chemistry of Solids

journal homepage: www.elsevier.com/locate/jpcs

Raman and first-principles study of the pressure-induced Mott-insulator to metal transition in bulk $FePS_3$

Subhadip Das [a,1], Shashank Chaturvedi [b,c,1], Debashis Tripathy [d], Shivani Grover [b,c], Rajendra Singh [c], D.V.S. Muthu [a], S. Sampath [d], U.V. Waghmare [b], A.K. Sood [a,*]

[a] Department of Physics, Indian Institute of Science, Bangalore, 560012, India
[b] Theoretical Sciences Unit, School of Advanced Materials, Jawaharlal Nehru Centre for Advanced Scientific Research, Bangalore, 560064, India
[c] Chemistry and Physics of Materials Unit, School of Advanced Materials, Jawaharlal Nehru Centre for Advanced Scientific Research, Bangalore, 560064, India
[d] Department of Inorganic and Physical Chemistry, Indian Institute of Science, Bangalore, 560012, India

ARTICLE INFO

Keywords:
Raman spectroscopy
High-pressure study
Mott insulator
Iron phosphorus trisulfide
Insulator-metal transition
Magnetic ordering

ABSTRACT

Members of a recently discovered class of two-dimensional materials based on transition metal phosphorous trichalcogenides exhibit an antiferromagnetic ground state and they have potential applications in spintronics. In particular, $FePS_3$ is a Mott insulator with a band gap of ~ 1.5 eV. In this study, we used Raman spectroscopy and first-principles density functional theoretical analysis to examine the stability of the structure and electronic properties of $FePS_3$ under pressure. Raman spectroscopy detected two phase transitions at 4.6 GPa and 12 GPa, which were characterized by changes in the pressure coefficients of the mode frequencies and the number of symmetry allowed modes. $FePS_3$ transformed from the ambient monoclinic C2/m phase with a band gap of 1.54 eV to another monoclinic C2/m (band gap of 0.1 eV) phase at 4.6 GPa, which was followed by another transition to the metallic trigonal P-31m phase at 12 GPa. Our findings complement those obtained recently in high pressure X-ray diffraction studies. The calculated elastic properties indicated increases in the bulk, shear, and Young's moduli, as well as a significant reduction in the universal elastic anisotropy index as the crystal changed from the ambient monoclinic C2/m phase to the high pressure trigonal P-31m phase.

1. Introduction

Transition metal phosphorus trichalcogenides ($TMPX_3$, where TM = Fe, Mn, Ni, or V, and X = S or Se) are a class of Mott insulators [1–4] with great potential applications as catalysts in the hydrogen evolution reaction [5], carbon dioxide reduction [6], batteries [7], photocatalysis [8], photodetectors [9,10], sensors [11,12], spintronics [13], and ultrathin magnetic devices [14–18]. $FePS_3$ is a member of this family that has a layered structure belonging to the monoclinic crystal system with the C2/m space group and a periodic unit cell containing two formula units [19]. Sulfur atoms follow ABCABC stacking along the *c* axis and the octahedral voids are occupied by P and Fe atoms [19]. Due to the low cleavage energy associated with the layered material, $FePS_3$ can be exfoliated down to a few layers by micromechanical cleavage and liquid exfoliation [5,9]. At a Néel temperature of T_N ~118 K, the material undergoes a phase transition from a paramagnet to a two-dimensional (2D) Ising-type zig-zag antiferromagnet (zAFM), with high spin moments (S = 2) for Fe^{2+} atoms pointing perpendicular to the basal plane of the lattice [20,21] (Fig. 1(a)). The Raman spectra below T_N contain additional modes due to lowering of the symmetry in the magnetic phase [20,22]. The presence of these modes down to a monolayer confirms the survival of antiferromagnetic (AFM) ordering in the 2D system with slight lowering in T_N due to weak interlayer van der Waals interactions [22].

Pressure is an excellent tool for tuning the structural, electronic [23–26], and topological [27] properties [24,25,28] of materials. First-principles calculations have been effectively used to understand the stability of materials through their electronic structure [29–31]. Although previous electronic band structure calculations for the bulk $FePS_3$ predicted its metallic nature [32], experiments confirmed the material as a Mott insulator with a band gap of ~ 1.5 eV, which is the lowest in the $TMPX_3$ family [33]. Recent high pressure X-ray diffraction (XRD) experiments at room temperature detected two phase transitions at ~ 4 GPa and ~ 14 GPa, where the first transition was from the

* Corresponding author.
E-mail address: asood@iisc.ac.in (A.K. Sood).
[1] Both authors contributed equally to this work.

https://doi.org/10.1016/j.jpcs.2022.110607
Received 20 September 2021; Received in revised form 22 January 2022; Accepted 23 January 2022
Available online 31 January 2022
0022-3697/© 2022 Elsevier Ltd. All rights reserved.

ambient C2/m phase to another C2/m phase and the second transition was to the metallic trigonal P-31m phase [4]. The carrier drift velocity and thermal performance of these high-pressure phases are affected by phonon renormalization, which can be analyzed in a non-invasive manner by using Raman spectroscopy. Furthermore, according to recent neutron-scattering measurements [34], the low pressure (LP) phase and the first high pressure (HP–I) phase of bulk $FePS_3$ between 6 and 14 GPa have distinct low-temperature magnetic structures comprising zAFM-I and zAFM-II, respectively (Fig. 1). Moreover, long-range magnetic ordering is lost in the second high-pressure phase (HP-II) between 14 and 18 GPa [34]. The relative stability, vibrational signatures, and nature of these magnetically ordered structures need to be understood better.

In this study, we conducted high pressure Raman experiments and density functional theory (DFT) based analysis of bulk $FePS_3$. Raman experiments detected two transitions at 4.6 GPa and 12 GPa, as shown by the pressure coefficients of the mode frequencies and significant changes in the number of modes, respectively. The linewidth of the phosphorus and sulfur dominated mode at $\sim$ 379 cm^{-1} exhibits an anomalous decrease with the pressure, which is attributable to the buckling of sulfur atoms. Our DFT + U calculations for the recently reported magnetic structures of bulk $FePS_3$ [34] showed that the HP-I phase has a narrow gap of $\sim$ 0.1 eV, thereby explaining the experimentally observed broadening of the linewidths for some of the Raman modes with pressure and the drop in resistivity above 5 GPa, as reported previously [4]. The HP-II phase is an ordinary metal without any long-range magnetic ordering. Comparisons of the experimentally determined pressure-dependent frequencies of the Raman modes and our calculations provide a clearer understanding of the transitions.

2. Experimental details

High quality and large sized single crystals of $FePS_3$ were synthesized by using the chemical vapor transport technique from the respective elements. Briefly, Fe, P, and S powders were prepared at a stoichiometric ratio of 1:1:3 and mixed well by grinding in an agate mortar. The mixture was transferred to a quartz tube (length of 20 cm and inner diameter of 18 mm) with iodine as the transport agent and sealed at a pressure of 2.7 $\times$ 10^{-5} mbar. The tube was then transferred to a two-zone furnace where the hot zone was kept at 900 °C and the cold zone at 850 °C. After conducting the reaction for two weeks, shiny black colored, centimeter-size crystals were obtained, which were used for further characterization. XRD patterns (see Fig. S1 of the supplementary information (SI)) were recorded using a PAN Analytical X-ray BV diffractometer with Cu Kα (1.541 8 Å) as the X-ray source.

A thin crystalline platelet of $FePS_3$ (dimension $\sim$ 100 μm), a small ruby chip, and a 16:3:1 volumetric solution of methanol, ethanol, and water, respectively, as the pressure transmitting medium were placed together on an indented stainless steel metal gasket in a hole with a diameter of $\sim$ 200 μm in a Mao–Bell type diamond-anvil cell. The doublet peaks of ruby fluorescence were used for pressure calibration. Room temperature Raman spectra were recorded in back-scattering geometry using a commercial Horiba LabRam HR-800 spectrometer coupled with a Peltier cooled charge-coupled device as the detector. A solid-state laser operating at a wavelength of 532 nm was focused on the crystal using a 50 $\times$ long working distance objective lens. The resolution of the captured spectra was $\sim$ 0.55 cm^{-1}. To avoid any unwanted heating or chemical reactions, the incident laser power was kept below 5 mW.

3. Computational details

We studied the pressure dependence of the structure, electronic properties, and phonons for $FePS_3$ using first-principles DFT, as implemented in the Quantum ESPRESSO software package [35]. In order to calculate the electronic and magnetic properties, we used the DFT + U method [36] with an effective on-site Coulomb repulsion parameter U = 2.5 eV for Fe 3d orbitals, as employed in a previous study [37]. The exchange-correlation energy of electrons was treated within a generalized gradient approximation and PBE functional [38,39]. An energy cut-off of 50 Ry was used when truncating basis sets to represent electronic wave functions and an energy cut-off of 400 Ry was used for charge density. $FePS_3$ belongs to the family of 2D materials with weak interactions between layers stacked along the c-axis, so we included Grimme-D2 dispersion corrections to account for van der Waals (vdW) pairwise $1/r^6$ interactions [40]. A uniform mesh of 6 $\times$ 4 $\times$ 3 k-points [41] was used for sampling Brillouin-zone (BZ) integrations when calculating the LP phase with zAFM-I magnetic ordering (see Fig. 1(a)). Similarly, a 6 $\times$ 4 $\times$ 6 mesh of k-points was used for sampling BZ for the HP-I phase with zAFM-II magnetic ordering (see Fig. 1(b)). Magnetic ordering of the HP-I phase was confirmed recently by Coak et al. in neutron-diffraction experiments [34]. In the calculations for the trigonal P-31m (HP-II) phase, a 6 $\times$ 6 $\times$ 6 mesh of k-points was used for sampling BZ integrations. Γ-point phonon modes were obtained using the frozen-phonon approach by maintaining the magnetic ordering of the reference LP and HP-I phases. Furthermore, we calculated the elastic

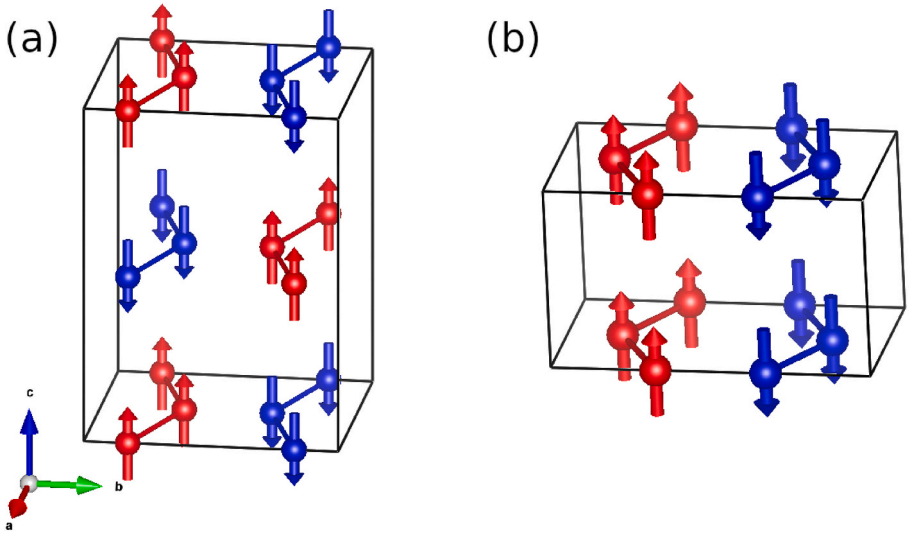

Fig. 1. Magnetic ordering of *C2/m* (a) LP (zAFM-I) and (b) HP-I (zAFM-II) phases [34]. P and S atoms are omitted and only the Fe atoms are shown. The figures were prepared using VESTA software [55].

constant matrix and universal anisotropy index to assess the mechanical stability of the phases of $FePS_3$ stabilized with pressure.

4. Results and discussion

4.1. Experimental results

In the absence of magnetic ordering, the bulk $FePS_3$ at ambient conditions belongs to the C2/m space group, thereby resulting in 30 zone center phonon modes ($\Gamma = 8A_g + 6A_u + 7B_g + 9B_u$) [22,42]. Fig. 2 shows the Raman modes for the bulk $FePS_3$ from 75 to 500 cm^{-1} at ambient pressure. The modes are labeled from L_1 to L_5, where the L_3 and L_5 modes are the A_g-modes, and L_2 and L_4 are combinations of the A_g and B_g modes [22,43]. The L_2 mode is iron dominated whereas the L_3, L_4 and L_5 modes originate from the molecular-like vibration of the $[P_2S_6]^{4-}$ unit [20,22]. The broad and asymmetric mode L_1 at ~ 130 cm^{-1} is reportedly an iron-dominated M-point phonon mode, which is resolved into multiple modes at T_N ~118 K due to anti-ferromagnetic ordering of the Fe atoms [20].

The changes in the Raman spectra at some representative pressures are shown in Fig. 2. Above 12 GPa, the modes are labeled as M_1 to M_8. The spectra were fitted with a sum of Lorentzian functions to extract the pressure evolution of the phonon frequencies (ω) (Fig. 3(a)) and linewidths (γ) (Fig. 4). The Raman lineshape of the L_1 mode is reported to be slightly asymmetric [20], but we simply used a Lorentzian fitting

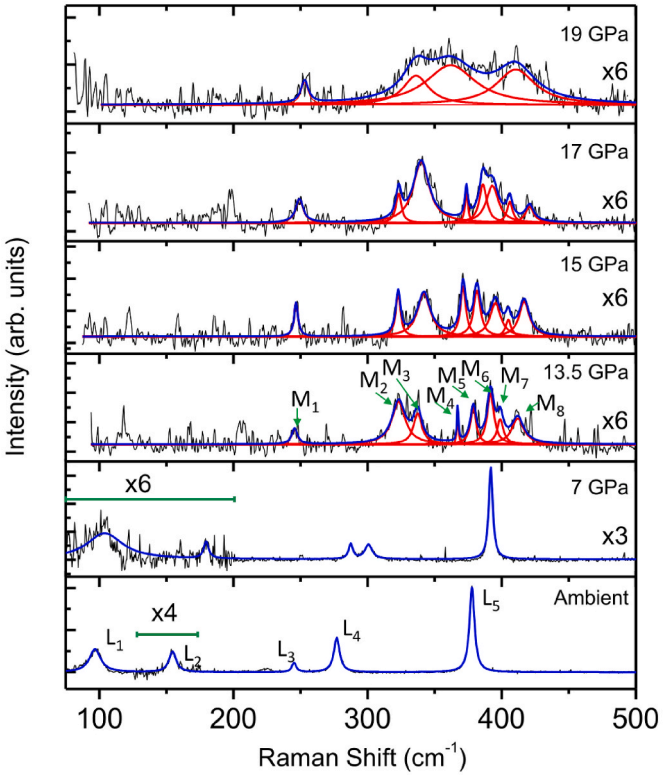

Fig. 2. Evolution of the Raman modes of bulk $FePS_3$ with pressure. Experimental data points are connected by black lines. Red and blue lines show the individual and cumulative Lorentzian peak fits, respectively. Modes are labeled in the figure. Intensities of some regions of the spectra are enhanced.

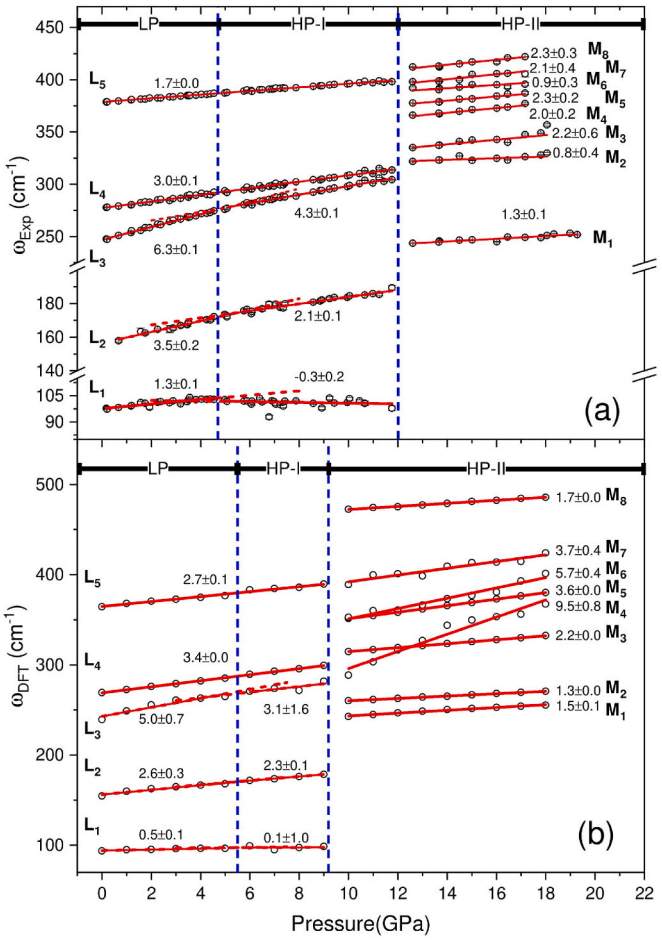

Fig. 3. (a) Experimentally observed and (b) theoretically calculated pressure evolution of Raman modes. The slopes for the red linear fit to the data are shown in the figure. The dashed red lines for the L_1, L_2, and L_3 modes represent extensions to their linear fits. The three structural phases are indicated in the figure and the corresponding transition pressures are highlighted by blue vertical dashed lines.

function to estimate the change in frequency with pressure. The modes L_1 to L_5 exhibited an expected linear increase in frequency with pressure, and they were fitted with the linear equation, $\omega(P) = \omega(P_0) + C(P - P_0)$, where $\omega(P_0)$ is the frequency at ambient pressure and C is the pressure coefficient. These fitting parameters are indicated in Fig. 3(a) and summarized in Table-I. Two transitions were identified at P_{C1} ~ 4.6 GPa and P_{C2} ~ 12 GPa. We observed significant decreases in the pressure coefficients C for the L_1, L_2, and L_3 modes above ~ 4.6 GPa, where the number of Raman modes remained the same. It was notable that the iron dominated L_1 mode had a negative pressure coefficient in the HP-I phase.

The first transition pressure P_{C1} is consistent with recent XRD measurements (~ 4 GPa) [4], and it can be attributed to a change in the crystal angle β from ~ 107° to ~ 90°, and a change in the atomic stacking of the iron and phosphorus atoms in the layer along the c* axis with higher inter-planar atomic coordination. Similar changes in the vibrational modes were also reported for $V_{0.9}PS_3$ at ~ 12 GPa, which leads to an insulator to metal transition [44]. We note that the L_1 mode remained a single peak throughout the LP and HP-I phases, thereby

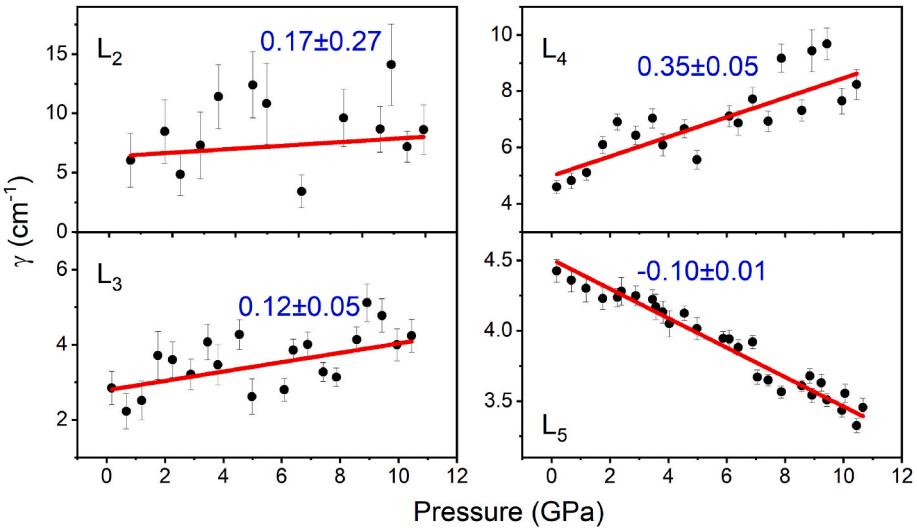

Fig. 4. Linewidth (γ) of the L_2, L_3, L_4, and L_5 modes with pressure. Red lines are the linear fits. The slope is shown near the lines in $cm^{-1}\cdot GPa^{-1}$ units.

indicating the absence of any AFM ordering at room temperature [20].

As shown in Figs. 2 and 3(a), the Raman spectra changed considerably above $P_{C2} \sim 12$ GPa, thereby indicating the second phase transition. Above ~ 12 GPa, eight distinct new modes were observed in the frequency range from 240 to 450 cm^{-1}. The transition pressure (P_{C2}) is very close to the reported C2/m to P-31m phase transition at ~ 14 GPa according to XRD measurements [4]. We note that the intensity of the Raman modes was reduced by almost half compared with the HP-I phase due to the metallic nature of the P-31m phase, as discussed in the next section. The frequencies of the Raman modes at 13 GPa and their pressure coefficients (C) are listed in Table-I. The M_4 to M_8 modes are close in terms of frequency, so we could analyze them up to 17 GPa, after which they became too broad for further analysis.

The intrinsic linewidth of the phonon modes provides information about phonon–phonon, electron–phonon, and spin–phonon interactions in a system [45]. Thus, as shown in Fig. 4, we analyzed the linewidths of the Raman modes from L_2 to L_5 in the LP and HP-1 phases with pressures up to the hydrostatic limit of our pressure transmitting medium (~ 10.5 GPa [46]). We do not comment on the linewidth of the L_1 mode because it is reportedly asymmetric and cannot be deconvoluted at ambient temperature [20]. The linewidths of the L_2, L_3, and L_4 modes increased with pressure. In the next section, we show that the HP-I phase is a narrow-gap semiconductor with a band gap of ~ 0.1 GPa. Previous transport measurements also showed that pressure induces significant reductions in resistivity above 5.5 GPa [4]. Thus, the electronic density of states at the Fermi level increased with pressure, leading to an increase in the EPC for the three modes. By contrast, the linewidth of the most intense L_5 mode with dominant vibrations of phosphorus and sulfur atoms exhibited an anomalous decrease with pressure, which can be attributed to the previously reported pressure-induced buckling of sulfur atoms due to a change in the stacking order along the c* axis [4]. The increased interaction between the sulfur atoms with pressure probably stabilized the L_5 mode, thereby leading to the gradual decrease in the linewidth. More theoretical research is needed to understand this effect. We note that for Bi_2Te_3 and Sb_2Se_3, similar anomalous Raman linewidths with pressure have been reported due to their electronic and structural transitions [27,47].

4.2. Theoretical analysis results

4.2.1. Transition pressures and electronic structure

We studied the pressure-dependent transitions based on first-principles calculations of the structures with appropriate magnetic ordering, as determined experimentally using neutron diffraction [34,48,49], as shown in Fig. 1. Previous theoretical studies considered zAFM-I magnetic ordering in their analysis of both the LP and HP-I phases [37,50], which is not consistent with a recent experimental demonstration of zAFM-II magnetic ordering in the HP-I phase [34]. Our calculations confirmed the experimental findings that zAFM-I and zAFM-II are the magnetic ground states of the HP-I and HP-II phases, respectively (see Table S1). The pressure dependences of the enthalpy difference (Fig. 5) of the LP (zAFM-I) and HP-I (zAFM-II) phases show that the C2/m (HP–I) phase is stabilized at pressures above $P_{c1} = 5.5$ GPa and the P-31m (HP-II) phase becomes stable at pressures above $P_{c2} =$ 9.2 GPa. These transition pressures are quite close to the experimental estimates obtained from Raman spectra, as discussed in the previous section. Neutron scattering experiments have shown that the HP-II phase has a short-range magnetic order, although precise magnetic ordering was not reported [34], which might explain the small underestimate of P_{c2} in our calculations where we assumed a non-magnetic ground state. The calculated lattice parameters are within the typical DFT errors (see Table S2) and in agreement with XRD experiments [4]. The structural transitions at P_{c1} and P_{c2} are associated with decreases in volume and the c-lattice parameter (Fig. S2). The estimate of the atomic moment on Fe at $P = 0$ GPa was calculated as 3.4 μ_B (Fig. 5(c)), which is close to the reported value of 3.5 μ_B [37].

We found phonon instabilities at the Γ-point of the LP phase, with the most unstable mode at 153i cm^{-1}, which is comparable to a recently reported calculation [50] of Γ-point instability at 100i cm^{-1}. The unstable modes of the LP phase are shown in Fig. S3. Importantly, distorting the structure along the eigenvectors of the unstable mode at 153i cm^{-1} stabilizes the structure and lowers its energy by 8 meV/f.u. The electronic properties of these structures do not change significantly, except for an increase in the band gap from 1.32 eV to 1.54 eV (Fig. S6). We found no unstable phonon modes in the HP-I and HP-II phases. The electronic structures of the LP, HP-I, and HP-II phases clearly

demonstrate that the LP phase is an insulator, while the HP-I phase has a narrow band gap of ~ 0.1 eV at *B*-point and the HP-II phase is metallic (Fig. 6). A notable reduction in the band gap from 1.54 eV to 0.1 eV across the LP to HP-I phase transition explains the significant drop

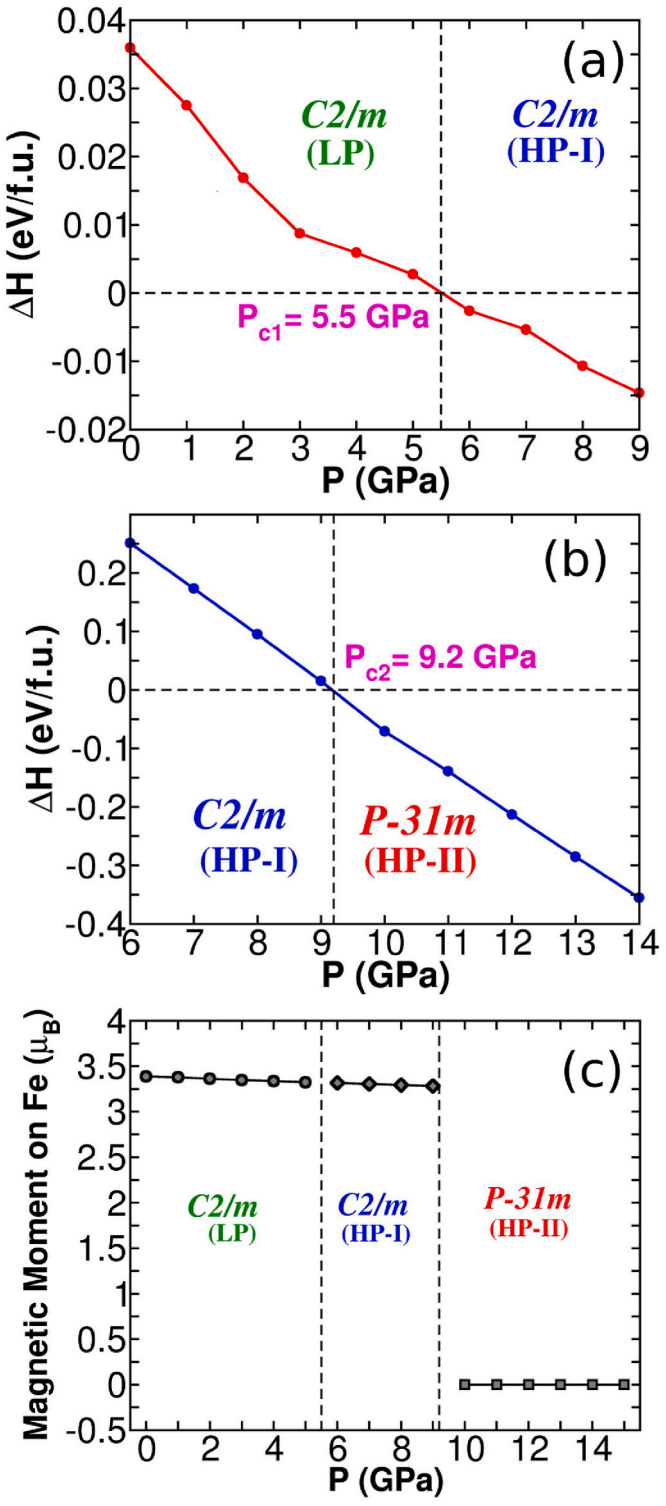

Fig. 5. Enthalpy curves showing the evolution of the crystal structure as a function of pressure. (a) P_{c1} = 5.5 GPa corresponds to the first structural transition from the LP to HP-I phase, and (b) P_{c2} = 9.2 GPa shows the transition to the high-pressure trigonal metallic phase. (c) Pressure dependence of calculated magnetic moments on Fe across phase transition. Calculations for the trigonal P-31m phase were performed based on a non-magnetic state.

observed in the resistivity from ~ 10^{11} $\mu\Omega cm$ at ambient (LP phase) to ~ 10^5 $\mu\Omega cm$ at 6.3 GPa (HP–I phase) [4,51,52]. The electronic structure clearly shows that pressure reduces the band gap in the HP-I phase (E_g ~ 0.1 eV) and eventually drives it to the metallic HP-II phase (Fig. 6). The projected density of states indicate hybridization of the Fe-*d* and P-*p* orbitals with S-*p* orbitals. In the HP-II phase, the Fe-*d*, P-*p*, and S-*p* orbitals contribute to the states at the Fermi level.

4.2.2. Calculated pressure dependence of Raman modes

We calculated the pressure dependences of the frequencies of phonons for the stable LP, HP-I, and HP-II phases using the frozen-phonon method. The unstable LP (zAFM-I) and HP-I (zAFM-II) phases have the C2/m space group, with 14 A_g and 16 B_g Raman modes, respectively. The displacement of atoms along the maximum instability in the LP phase breaks the symmetry of the structure, which can be understood based on the overlap of the A_g and B_g phonon mode eigenvectors of the unstable structure with the phonon mode eigenvectors of the stable structure of the LP phase (Fig. S9). Thus, structural distortion leads to non-zero overlap between multiple modes. In all three phases, the direction of the *c*-axis is perpendicular to the layers. The calculated mode frequencies as a function of pressure (Fig. 3(b)) and their pressure coefficients (*C*) (Table 1) are close to the experimental values. In the LP phase, three low-frequency Raman active B_g modes are observed (Fig. S5). The B_g mode at 54 cm^{-1} (Fig. S5(c)) involves displacement of individual monolayers against each other along the *c*-axis. This mode increases in frequency by ~ 48 cm^{-1} after changing from 0 to 5 GPa, which is much larger than the changes in the modes at 25 cm^{-1} and 26 cm^{-1} (Figs. S5(a) and S5(b)). The B_g modes at 25 cm^{-1} and 26 cm^{-1}, where monolayers slide against each other along the *b* and *a*-directions, respectively, exhibit a weaker increase of ~ 18 cm^{-1} from 0 to 5 GPa (Fig. S5(a)). However, the increases in the mode frequencies decline with pressure due to the reduced vdW gap between the layers at high pressures. The L_1 mode of the LP and HP-I phases has a relatively low *C* value because they only involve out-of-plane vibrations by Fe atoms (Figs. S4(a) and S7(a)), and are not significantly affected by changes in the vdW gap. The L_3 mode in the LP phase has the highest *C* value of ~ 5 $cm^{-1}GPa^{-1}$, which decreases to ~ 3 $cm^{-1}GPa^{-1}$ in the HP-I phase. This is understandable because the L_3 mode only involves vibrations of S atoms along the layered direction. For both the L_2 and L_3 modes, there is a change in the pressure coefficient above P_{c1}. The L_4 and L_5 modes exhibit no changes in *C* across the P_{c1} transition (Table 1). The L_2, L_4, and L_5 modes of the LP and HP-I phases involve displacements of P and S atoms, and thus the *C* values are higher than that for the L_1 mode with Fe vibrations but lower than that for the L_3 mode.

The HP-II phase has eight Raman active modes (5 E_g+3 A_{1g}). Comparisons of the experimental and calculated frequencies at 13 GPa show that some of the observed modes cannot be assigned to the calculated frequencies (Table 1). We note that our calculations for the phonons at 18 GPa are in agreement with previous theoretical results (Table S3) [53]. The E_g modes involve in-plane vibrations of Fe, P, and S atoms, whereas the A_{1g} modes involve the vibrations of P and S atoms against each other along the *c*-direction (Fig. S8). Fig. 3(b) clearly shows that the pressure coefficient is weaker for the E_g modes in the HP-II phase than the A_{1g} modes.

4.2.3. Mechanical properties

To assess the mechanical stabilities of the three phases of $FePS_3$ stabilized enthalpically with pressure, we determined the bulk modulus (K), shear modulus (G), and Young's modulus (Y) for the LP (at 0 GPa), HP-I (at 8 GPa), and HP-II (at 14 GPa) phases. The Voigt and Reuss approximations give the upper and lower bounds, respectively, for K, G, and Y, and the Voigt–Reuss–Hill average is expected to be closer to the experimental values. The results in Table 2 clearly show that K, G, and Y increase as the crystal structure changes from LP → HP-I → HP-II, which may be associated with the decreasing vdW gap under pressure. Furthermore, we determined the universal elastic anisotropy index (A^U

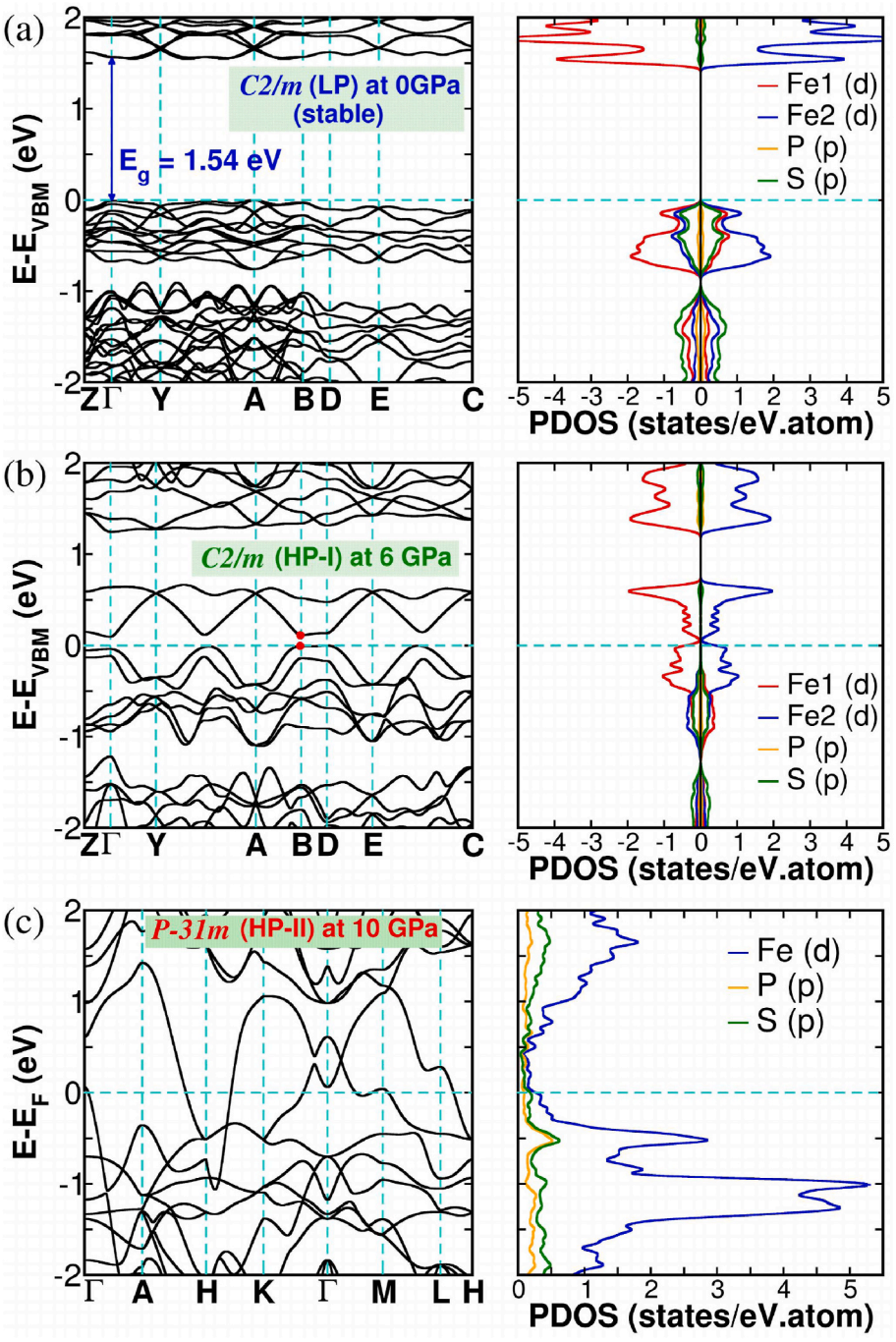

Fig. 6. Electronic structure and projected density of states for the LP, HP-I, and HP-II phases of $FePS_3$. In the LP phase, a band gap of 1.54 eV at the Γ-point is observed, which decreased to ~ 0.1 eV at the *B*-point in the HP-I phase (shown by red dots) stabilized under pressure. The HP-II phase is metallic with finite contributions of the Fe-*d*, P-*p*, and S-*p* orbitals to the states at the Fermi level.

$= 5(G_V/G_R) + (K_V/K_R) - 6 \geq 0$), which quantifies the anisotropy of a material [54], i.e., a material is more anisotropic when the value of A^U is higher. We found that the LP (C2/m) phase has the largest A^U but it is much lower for the HP-I (C2/m) phase ($A^U = 1.9$) and lowest for the high symmetry trigonal HP-II (P-31m) phase ($A^U = 0.5$) [Table II].

5. Conclusions

In this study, we analyzed the electronic and vibrational properties of bulk $FePS_3$ as a function of pressure based on Raman spectroscopy and first-principles calculations. We observed a structural phase transition at $P_c \sim 4.6$ GPa, which is marked by reductions in the pressure coefficients for the Raman modes near 98 cm^{-1}, 158 cm^{-1}, and 248 cm^{-1}. This is accompanied by broadening of the linewidths for the L_2, L_3, and L_4 Raman modes up to 10.5 GPa due to an increase in the EPC. By contrast, the linewidth of the sulfur and phosphorus dominated mode L_5 exhibits an anomalous decrease with pressure, probably due to the previously reported buckling of the sulfur atoms. Eight new Raman modes were observed in the frequency range from 240 to 412 cm^{-1} in the P-31m phase above 12 GPa. Our DFT + *U* calculations indicate that the LP phase is an insulator with an electronic gap of 1.54 eV, which reduces dramatically to ~ 0.1 eV in the HP-I phase and the HP-II phase is metallic. Our calculated values of the transition pressures are close to the estimates obtained from Raman and XRD experiments. The

Table 1
Comparison of the experimentally observed and theoretically calculated phonon frequency (ω) and pressure coefficient (C) of the Raman active modes in the three structural phases of $FePS_3$. Changes in C are shown for the L_1, L_2, and L_3 modes through the LP and HP-I phases.

Structure	Modes	Symmetry	Frequency (cm^{-1})		Pressure coefficient ($cm^{-1}GPa^{-1}$)	
			ω_{Exp} (0 GPa)	ω_{DFT} (0 GPa)	C_{Exp}	C_{DFT}
C2/m (LP)	L_1	A_g, B_g	97.8 ± 0.4	94	1.3 ± 0.1	0.5 ± 0.1
	L_2	A_g	158.5 ± 0.6	154	3.5 ± 0.2	2.6 ± 0.3
	L_3	A_g	247.7 ± 0.3	239	6.3 ± 0.1	5.0 ± 0.7
	L_4	A_g, B_g	278.0 ± 0.2	269	3.0 ± 0.1	3.4 ± 0.0
	L_5	A_g	378.6 ± 0.2	365	1.7 ± 0.0	2.7 ± 0.1
			ω_{Exp} (6 GPa)	ω_{DFT} (6 GPa)		
C2/m (HP–I)	L_1	B_g	100.1 ± 0.7	99	−0.3 ± 0.2	0.1 ± 1.0
	L_2	B_g	173.8 ± 0.6	172	2.1 ± 0.1	2.3 ± 0.1
	L_3	A_g	281.5 ± 0.2	271	4.3 ± 0.1	3.1 ± 1.6
	L_4	B_g	295.3 ± 0.2	290	3.0 ± 0.1	3.4 ± 0.0
	L_5	A_g	389.7 ± 0.0	383	1.7 ± 0.0	2.7 ± 0.1
			ω_{Exp} (13 GPa)	ω_{DFT} (13 GPa)		
P-31m (HP-II)	M_1	E_g	248.5 ± 2.3	259	1.3 ± 0.1	1.5 ± 0.1
	M_2	E_g	322.2 ± 6.4	264	0.8 ± 0.4	1.3 ± 0.0
	M_3	E_g	335.2 ± 9.6	321	2.2 ± 0.6	2.2 ± 0.0
	M_4	A_{1g}	365.2 ± 2.6	327	2.3 ± 0.2	9.5 ± 0.8
	M_5	E_g	377.3 ± 3.3	362	2.0 ± 0.2	3.6 ± 0.0
	M_6	A_{1g}	389.8 ± 5.2	366	1.6 ± 0.4	5.7 ± 0.4
	M_7	A_{1g}	397.2 ± 4.7	399	2.1 ± 0.3	3.7 ± 0.4
	M_8	E_g	411.2 ± 2.8	477	2.3 ± 0.2	1.7 ± 0.0

frequencies and pressure coefficients of the Raman modes calculated for the LP and HP-I monoclinic phases are in qualitative agreement with our experimental results. However, exact knowledge of experimentally reported short-range magnetic ordering in the HP-II trigonal phase is needed to explain the nature of its phonon modes in detail and to obtain a better estimate of P_{c2}. Symmetry analysis of the phonon eigenvectors indicates that the L_3 mode in the LP phase and A_{1g} modes in the HP-II phase have relatively higher pressure coefficients. These modes involve vibrations of P and S atoms along the layered direction. Our estimates of the bulk, shear, and Young's moduli clearly demonstrate that they increase with pressure as the crystal structure changes from LP → HP-I → HP-II, and the universal elastic anisotropy index decreases dramatically from the monoclinic LP phase to the trigonal HP-II phase. We hope that our findings facilitate future applications of $FePS_3$ and other $TMPX_3$ compounds in ultrathin novel magnetic devices.

Table 2
Elastic moduli and anisotropy of the three phases of $FePS_3$. The universal anisotropy index (A^U) was determined as described previously [54]. Bulk, shear, and Young's moduli increase with the structural transitions, and the universal elastic anisotropic index A^U decreases significantly through the transitions from the low symmetry C2/m phases (LP and HP-I) to the high symmetry trigonal P-31m (HP-II) phase.

Property	Unit	LP	HP-I	HP-II
Young's modulus Voigt average (Y_V)	GPa	76	115	237
Young's modulus Reuss average (Y_R)	GPa	26	88	220
Young's modulus Voigt—Reuss–Hill (VRH) average (Y_{VRH})	GPa	51	102	229
Bulk modulus Voigt average (K_V)	GPa	58	81	162
Bulk modulus Reuss average (K_R)	GPa	24	72	137
Bulk modulus Voigt–Reuss–Hill (VRH) average (K_{VRH})	GPa	41	77	150
Shear modulus Voigt average (G_V)	GPa	30	46	94
Shear modulus Reuss average (G_R)	GPa	9	34	89
Shear modulus Voigt–Reuss–Hill (VRH) average (G_{VRH})	GPa	20	40	92
Universal elastic anisotropy (A^U)	–	13.1	1.9	0.5

Credit author statement

Subhadip Das: Methodology, Formal analysis, Investigation, Visualization, Data Curation, Validation, Writing - Original Draft. **Shashank Chaturvedi:** Software, Formal analysis, Methodology, Investigation, Visualization, Data Curation, Validation, Writing - Original Draft. **Debashis Tripathy:** Resources, Validation, Formal analysis, Writing - Original Draft. **Shivani Grover:** Software, Formal analysis, Visualization. **Rajendra Singh:** Software. **D. V. S. Muthu:** Methodology, Validation, Supervision, Conceptualization, Writing - Review & Editing. **S. Sampath:** Methodology, Validation, Supervision, Writing - Review & Editing. **U. V. Waghmare:** Methodology, Validation, Supervision, Conceptualization, Writing - Review & Editing, Project administration, Funding acquisition. **A. K. Sood:** Methodology, Validation, Supervision, Conceptualization, Writing - Review & Editing, Project administration, Funding acquisition.

Data availability statement

The data that support the findings obtained in this study are available from the corresponding author upon reasonable request.

Declaration of competing interest

The authors declare that they have no known competing financial interests or personal relationships that could have appeared to influence the work reported in this paper.

Acknowledgments

A.K.S. thanks Department of Science and Technology, India for support under the Year of Science Professorship and Nanomission Council. S.C. acknowledges JNCASR for a research fellowship and Thematic Unit of Excellence on Computational Material Science, JNCASR for computational resources. U.V.W. acknowledges support from a J.C. Bose National fellowship of SERB-DST, Govt. of India.

Appendix A. Supplementary data

Supplementary data to this article can be found online at https://doi.org/10.1016/j.jpcs.2022.110607.

References

[1] M.H. Whangbo, R. Brec, G. Ouvrard, J. Rouxel, Inorg. Chem. 24 (1985) 2459.
[2] V. Grasso, L. Silipigni, Nuovo Cimento Rivista Serie (2002) 1, 025.
[3] V. Zhukov, S. Alvarez, D. Novikov, J. Phys. Chem. Solid. 57 (1996) 647.
[4] C.R.S. Haines, M.J. Coak, A.R. Wildes, G.I. Lampronti, C. Liu, P. Nahai-Williamson, H. Hamidov, D. Daisenberger, S.S. Saxena, Phys. Rev. Lett. 121 (2018) 266801.
[5] D. Mukherjee, P.M. Austeria, S. Sampath, ACS Energy Lett. 1 (2016) 367.
[6] L. Ji, L. Chang, Y. Zhang, S. Mou, T. Wang, Y. Luo, Z. Wang, X. Sun, ACS Catal. 9 (2019) 9721.
[7] Y. Fujii, A. Miura, N.C. Rosero-Navarro, M. Higuchi, K. Tadanaga, Electrochim. Acta 241 (2017) 370.
[8] Z. Cheng, T.A. Shifa, F. Wang, Y. Gao, P. He, K. Zhang, C. Jiang, Q. Liu, J. He, Adv. Mater. 30 (2018) 1707433.
[9] M. Ramos, F. Carrascoso, R. Frisenda, P. Gant, S. Mañas-Valero, D.L. Esteras, J. J. Baldoví, E. Coronado, A. Castellanos-Gomez, M.R. Calvo, npj 2D Materials and Applications 5 (2021) 19.
[10] R. Kumar, R.N. Jenjeti, M.P. Austeria, S. Sampath, J. Mater. Chem. C 7 (2019) 324.
[11] R. Kumar, R.N. Jenjeti, S. Sampath, ACS Sens. 5 (2020) 404, pMID: 31975587.
[12] R.N. Jenjeti, R. Kumar, S. Sampath, J. Mater. Chem. 7 (2019) 14545.
[13] X. Li, X. Wu, J. Yang, J. Am. Chem. Soc. 136 (2014) 11065.
[14] J.S. Evans, D. O'Hare, R. Clement, A. Leaustic, P. Thuéry, Adv. Mater. 7 (1995) 735.
[15] R. Clement, J.J. Girerd, I. Morgenstern-Badarau, Inorg. Chem. 19 (1980) 2852.
[16] G. Le Flem, R. Brec, G. Ouvard, A. Louisy, P. Segransan, J. Phys. Chem. Solid. 43 (1982) 455.
[17] P.A. Joy, S. Vasudevan, Phys. Rev. B 46 (1992) 5425.
[18] S. Bénard, A. Léaustic, E. Rivière, P. Yu, R. Clément, Chem. Mater. 13 (2001) 3709.
[19] R. Brec, Solid State Ionics 22 (1986) 3.
[20] J.-U. Lee, S. Lee, J.H. Ryoo, S. Kang, T.Y. Kim, P. Kim, C.-H. Park, J.-G. Park, H. Cheong, Nano Lett. 16 (2016) 7433.
[21] D. Lançon, H.C. Walker, E. Ressouche, B. Ouladdiaf, K.C. Rule, G.J. McIntyre, T. J. Hicks, H.M. Rønnow, A.R. Wildes, Phys. Rev. B 94 (2016) 214407.
[22] X. Wang, K. Du, Y.Y.F. Liu, P. Hu, J. Zhang, Q. Zhang, M.H.S. Owen, X. Lu, C. K. Gan, P. Sengupta, C. Kloc, Q. Xiong, 2D Mater. 3 (2016), 031009.
[23] S.N. Gupta, A. Singh, K. Pal, D.V.S. Muthu, C. Shekhar, Y. Qi, P.G. Naumov, S. A. Medvedev, C. Felser, U.V. Waghmare, A.K. Sood, Phys. Rev. B 97 (2018), 064102.
[24] S.N. Gupta, A. Singh, S. Sarkar, D.V.S. Muthu, S. Sampath, U. Waghmare, A. K. Sood, Phys. Rev. B 101 (2020), 035123.
[25] X.-M. Zhao, H.-y. Liu, A.F. Goncharov, Z.-W. Zhao, V.V. Struzhkin, H.-K. Mao, A. G. Gavriliuk, X.-J. Chen, Phys. Rev. B 99 (2019), 024111.
[26] Y. Qi, P.G. Naumov, M.N. Ali, C.R. Rajamathi, W. Schnelle, O. Barkalov, M. Hanfland, S.-C. Wu, C. Shekhar, Y. Sun, et al., Nat. Commun. 7 (2016) 1.
[27] A. Bera, K. Pal, D.V.S. Muthu, S. Sen, P. Guptasarma, U.V. Waghmare, A.K. Sood, Phys. Rev. Lett. 110 (2013) 107401.
[28] S.N. Gupta, A. Singh, K. Pal, B. Chakraborti, D.V.S. Muthu, U.V. Waghmare, A. K. Sood, Phys. Rev. B 96 (2017), 094104.
[29] L. Fu, R. Wang, C. Zhao, J. Huo, C. He, K.-H. Kim, W. Zhang, Chem. Eng. J. 414 (2021) 128857.
[30] C. He, R. Sun, L. Fu, J. Huo, C. Zhao, X. Li, Y. Song, S. Wang, Chin. Chem. Lett. (2021), https://doi.org/10.1016/j.cclet.2021.05.072.
[31] J. Yu, C. He, C. Pu, L. Fu, D. Zhou, K. Xie, J. Huo, C. Zhao, L. Yu, Chin. Chem. Lett. 32 (2021) 3149.
[32] A. Hashemi, H.-P. Komsa, M. Puska, A.V. Krasheninnikov, J. Phys. Chem. C 121 (2017) 27207.
[33] K.-z. Du, X.-z. Wang, Y. Liu, P. Hu, M.I.B. Utama, C.K. Gan, Q. Xiong, C. Kloc, ACS Nano 10 (2016) 1738.
[34] M.J. Coak, D.M. Jarvis, H. Hamidov, A.R. Wildes, J.A.M. Paddison, C. Liu, C.R. S. Haines, N.T. Dang, S.E. Kichanov, B.N. Savenko, S. Lee, M. Kratochvílová, S. Klotz, T.C. Hansen, D.P. Kozlenko, J.-G. Park, S.S. Saxena, Phys. Rev. X 11 (2021), 011024.
[35] P. Giannozzi, S. Baroni, N. Bonini, M. Calandra, R. Car, C. Cavazzoni, D. Ceresoli, G.L. Chiarotti, M. Cococcioni, I. Dabo, A.D. Corso, S. de Gironcoli, S. Fabris, G. Fratesi, R. Gebauer, U. Gerstmann, C. Gougoussis, A. Kokalj, M. Lazzeri, L. Martin-Samos, N. Marzari, F. Mauri, R. Mazzarello, S. Paolini, A. Pasquarello, L. Paulatto, C. Sbraccia, S. Scandolo, G. Sclauzero, A.P. Seitsonen, A. Smogunov, P. Umari, R.M. Wentzcovitch, J. Phys. Condens. Matter 21 (2009) 395502.
[36] M. Cococcioni, S. de Gironcoli, Phys. Rev. B 71 (2005), 035105.
[37] Y. Zheng, X.-x. Jiang, X.-x. Xue, J. Dai, Y. Feng, Phys. Rev. B 100 (2019) 174102.
[38] X. Hua, X. Chen, W.A. Goddard, Phys. Rev. B 55 (1997) 16103.
[39] J.P. Perdew, K. Burke, M. Ernzerhof, Phys. Rev. Lett. 77 (1996) 3865.
[40] S. Grimme, J. Comput. Chem. 27 (2006) 1787.
[41] P. Wisesa, K.A. McGill, T. Mueller, Phys. Rev. B 93 (2016) 155109.
[42] A. Hashemi, H.-P. Komsa, M. Puska, A.V. Krasheninnikov, J. Phys. Chem. C 121 (2017) 27207.
[43] M. Bernasconi, G.L. Marra, G. Benedek, L. Miglio, M. Jouanne, C. Julien, M. Scagliotti, M. Balkanski, Phys. Rev. B 38 (1988) 12089.
[44] M.J. Coak, Y.-H. Kim, Y.S. Yi, S. Son, S.K. Lee, J.-G. Park, Phys. Rev. B 100 (2019), 035120.
[45] N. Bonini, M. Lazzeri, N. Marzari, F. Mauri, Phys. Rev. Lett. 99 (2007) 176802.
[46] S. Klotz, J.-C. Chervin, P. Munsch, G.L. Marchand, J. Phys. Appl. Phys. 42 (2009), 075413.
[47] F.J. Manjón, R. Vilaplana, O. Gomis, E. Pérez-González, D. Santamaría-Pérez, V. Marín-Borrás, A. Segura, J. González, P. Rodríguez-Hernández, A. Muñoz, C. Drasar, V. Kucek, V. Muñoz-Sanjosé, physica status solidi (b) 250 (2013) 669.
[48] G. Le Flem, R. Brec, G. Ouvard, A. Louisy, P. Segransan, J. Phys. Chem. Solid. 43 (1982) 455.
[49] K. Kurosawa, S. Saito, Y. Yamaguchi, J. Phys. Soc. Jpn. 52 (1983) 3919.
[50] F. Kargar, E.A. Coleman, S. Ghosh, J. Lee, M.J. Gomez, Y. Liu, A.S. Magana, Z. Barani, A. Mohammadzadeh, B. Debnath, R.B. Wilson, R.K. Lake, A.A. Balandin, ACS Nano 14 (2020) 2424.
[51] K. Ichimura, M. Sano, Synth. Met. 45 (1991) 203.
[52] M.J. Coak, D.M. Jarvis, H. Hamidov, C.R.S. Haines, P.L. Alireza, C. Liu, S. Son, I. Hwang, G.I. Lampronti, D. Daisenberger, P. Nahai-Williamson, A.R. Wildes, S. S. Saxena, J.-G. Park, J. Phys. Condens. Matter 32 (2019) 124003.
[53] R.A. Evarestov, A. Kuzmin, J. Comput. Chem. 41 (2020) 1337.
[54] S.I. Ranganathan, M. Ostoja-Starzewski, Phys. Rev. Lett. 101 (2008), 055504.
[55] K. Momma, F. Izumi, J. Appl. Crystallogr. 44 (2011) 1272.